J Neuropathol Exp Neurol
Vol. 00, No. 00, 2020, pp. 1–10
doi: 10.1093/jnen/nlaa131

ORIGINAL ARTICLE

Hemodynamic Force as a Potential Regulator of Inflammation-Mediated Focal Growth of Saccular Aneurysms in a Rat Model

Kampei Shimizu, MD, Hiroharu Kataoka, MD, PhD, Hirohiko Imai, MD, PhD, Yuto Yamamoto, BS, Tomohiro Yamada, BS, Haruka Miyata, MD, PhD, Hirokazu Koseki, MD, PhD, Yu Abekura, MD, Mieko Oka, MD, Mika Kushamae, MD, Isao Ono, MD, Susumu Miyamoto, MD, PhD, Masanori Nakamura, MD, PhD, and Tomohiro Aoki, MD, PhD

Abstract

Past studies have elucidated the crucial role of macrophage-mediated inflammation in the growth of intracranial aneurysms (IAs), but the contributions of hemodynamics are unclear. Considering the size of the arteries, we induced de novo aneurysms at the bifurcations created by end-to-side anastomoses with the bilateral common carotid arteries in rats. Sequential morphological data of induced aneurysms were acquired by magnetic resonance angiography. Computational fluid dynamics analyses and macrophage imaging by ferumoxytol were performed. Using this model, we found that de novo saccular aneurysms with a median size of 3.2 mm were induced in 20/45 (44%) of animals. These aneurysms mimicked human IAs both in morphology and pathology. We detected the focal growth of induced aneurysms between the 10th and 17th day after the anastomosis. The regional maps of hemodynamic parameters demonstrated the area exposed to low wall shear stress (WSS) and high oscillatory shear index (OSI) colocalized with the regions of growth. WSS values were significantly lower in the growing regions than in ones without growth. Macrophage imaging showed colocalization of macrophage infiltration with the growing regions. This experimental model demonstrates the potential contribution of low WSS and high OSI to the macrophage-mediated growth of saccular aneurysms.

Key Words: Animal model, Computational fluid dynamics, Growth, Intracranial aneurysm, Macrophage.

INTRODUCTION

Aneurysms are vascular diseases characterized by outward bulging in various sizes of arteries (e.g. the aorta, intracranial arteries, and visceral arteries) (1–3). Management of these aneurysms is clinically important because of the high morbidity and mortality associated with aneurysmal bleeds (4). For the management of intracranial aneurysms (IAs), the development of diagnostic tools to distinguish rupture-prone IAs among stable ones has been a central goal for the field. The understanding of mechanisms underlying the growth of IAs is relevant because estimated rupture rates are high in enlarging human IAs (5, 6).

Experimental studies using animal models have elucidated the crucial role of nuclear factor-kappa B (NF-κB)-mediated chronic inflammation in the growth of IAs (7, 8). Furthermore, infiltrating macrophages have been highlighted as a major type of cells regulating the chronic inflammation in IAs (9, 10). Meanwhile, recent studies by computational fluid dynamics (CFD) analyses of human IAs have revealed the correlation of some hemodynamic parameters with initiation or rupture of IAs (11). The precise contribution of hemodynamics to the macrophage-mediated growth of aneurysms, however, remains to be elucidated.

Unfortunately, the diameters of intracranial arteries in established animal models are too small (∼100 μm) to be visualized in detail by radiological modalities, such as magnetic

From the Department of Molecular Pharmacology, Research Institute, National Cerebral and Cardiovascular Center, Suita (KS, HM, HKo, YA, MO, MK, IO, TA); Department of Neurosurgery, Kyoto University Graduate School of Medicine, Kyoto (KS, HKa, YA, IO, SM); Core Research for Evolutional Science and Technology (CREST) from Japan Agency for Medical Research and Development (AMED), National Cerebral and Cardiovascular Center, Suita (KS, HM, HKo, YA, MO, MK, IO, TA); Department of Systems Science, Graduate School of Informatics, Kyoto University, Kyoto (HI); and Department of Mechanical Engineering, Nagoya Institute of Technology, Nagoya (YY, TY, MN), Japan.

Send correspondence to: Tomohiro Aoki, MD, PhD, Department of Molecular Pharmacology, Research Institute, National Cerebral and Cardiovascular Center, 6-1 Kishibeshinmachi, Suita City, Osaka 564-8565, Japan; E-mail: tomoaoki@ncvc.go.jp

This study was supported by Core Research for Evolutional Science and Technology (CREST) on Mechanobiology from the Japan Agency for Medical Research and Development (AMED) (Grant ID: JP18gm0810006, JP19gm081006, JP20gm081006 to T.A.), and Grant-in-Aid for Scientific Research from the Ministry of Education, Culture, Sports, Science and Technology of Japan (#19H04455 and #18K12055 to M.N.). M.K. was supported by CREST from AMED (Grant ID: JP18gm0810006, JP19gm081006 to T.A.).

The authors have no duality or conflicts of interest to declare.

Supplementary Data can be found at academic.oup.com/jnen.

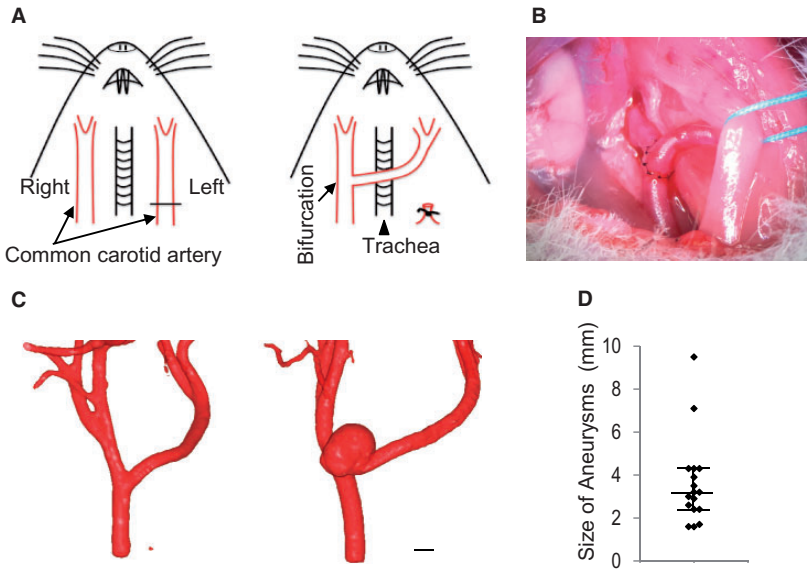

FIGURE 1. Present aneurysm model in rats. **(A)** Schematic representation of surgical procedures. The bar indicated by an arrowhead in the left panel shows the site where the left common carotid artery (CCA) is cut. **(B)** The macroscopic image of the surgically created CCA bifurcation. **(C)** Representative MR angiographies of the CCA bifurcation with (right) or without (left) an aneurysm lesion. Scale bar: 1 mm. **(D)** The size (n = 17) of induced aneurysms at the surgically created CCA bifurcation.

resonance angiography (MRA). Analyses of the hemodynamic forces imposed on lesions have thus been limited in these models (12). In this study, we established an aneurysm model at the common carotid artery (CCA) in rats because the diameter of this artery is ~10 times larger (~1 mm) than that of intracranial arteries and thereby sufficiently large for CFD analyses. We examined potential hemodynamic factors regulating the growth and their association with macrophage infiltration in these lesions.

MATERIALS AND METHODS

The animal experiments complied with the National Institute of Health's Guide for the Care and Use of Laboratory Animals and the Animal Research Reporting In Vivo Experiments (ARRIVE) guidelines. The Institutional Animal Care and Use Committee of our institutions approved the protocol.

Rat Aneurysm Model

Seven-week-old male Sprague-Dawley rats were purchased from Japan SLC (Shizuoka, Japan). Rats were maintained on a light/dark cycle of 12 hour/12 hour and had free access to chow and water. A total of 63 animals was subjected to the present aneurysm model (Fig. 1A). Under general anesthesia by intraperitoneal injection of pentobarbital sodium (50 mg/kg) and inhalation of isoflurane (1.5%–2.0%), the left CCA was cut in the proximal portion and moved to the right side. The left CCA was then anastomosed to the right CCA in an end-to-side fashion to create a bifurcation with a 10-0 nylon suture (Fig. 1A, B). Increase in hemodynamic stress due to hypervolemia was also induced by salt overloading and ligation of the left renal artery. Blood pressure was measured by the tail-cuff method preoperatively and on the 10th day after the aneurysm induction. Immediately after the surgical manipulations, animals were fed the chow containing 8% sodium chloride and 0.12% 3-aminopropionitrile (Tokyo Chemical Industry, Tokyo, Japan), an inhibitor of lysyl oxidase that catalyzes the cross-linking of collagen and elastin. Sham operations were performed in 6 rats as follows: A linear incision (2 mm) and sutures were performed at the anterior wall of the bilateral CCAs with a combination of the administration of 3-aminopropionitrile, salt overloading, and ligation of the left renal artery as described above.

Because the diameter of the parent artery is ~1 mm, we defined the onset of saccular aneurysms in this model as an outward bulging, reaching >1 mm in the largest dimension.

Histological Analysis and Immunohistochemistry

For histological analyses, animals were transcardially perfused with 4% paraformaldehyde solution after their death by intraperitoneal administration of a lethal dose of pentobarbital sodium (200 mg/kg). The CCA bifurcation with the induced aneurysm lesion was then harvested and 4-μm-thick paraffin sections were prepared.

Histopathological examinations were done using Elastic van Gieson staining. Immunohistochemical analyses were performed as previously described (8). Briefly, at the indicated period after surgical manipulation, 4-μm-thick paraffin sections were prepared from dissected aneurysm lesions and surrounding arterial walls, as described above. After blocking with 3% donkey serum (Jackson ImmunoResearch, West Grove, PA), slices were incubated with primary antibodies followed by incubation with secondary antibodies conjugated

with a fluorescence dye (Jackson ImmunoResearch). Finally, fluorescent images were acquired on a confocal fluorescence microscope system (FV1000, Olympus, Tokyo, Japan). To quantitate the presence of inflammatory cells and the expression of molecules examined, the cell counts per mm^2 or percentage of area positive for staining was assessed by setting a region of interest of 300 μm^2 in the area where positive signals were most abundantly observed.

The following primary antibodies were used: Mouse monoclonal anti-α-smooth muscle actin antibody (Sigma-Aldrich, St. Louis, MO, clone 1A4, 1:200), rabbit monoclonal anti-CD31 antibody (Abcam, Cambridge, UK, clone EPR17259, 1:2000), mouse monoclonal anti-CD68 antibody (Abcam, clone ED1, 1:50), mouse monoclonal anti-NF-κB, p65 subunit, active form, antibody (MERCK, Darmstadt, Germany, clone 12H11, 1:100), rabbit polyclonal anti-inducible nitric oxide synthase antibody (Abcam, ab15323, 1:100), rabbit polyclonal anti-matrix metalloproteinase 9 antibody (Abcam, ab38898, 1:100), and rabbit polyclonal anti-myeloperoxidase antibody (Abcam, ab9535, 1:100).

MRI Experiments

A 7-T preclinical scanner (BioSpec 70/20 USR; Bruker BioSpin MRI, Ettlingen, Germany) was used. Morphological information was acquired by 3D time-of-flight MRA (3D TOF-MRA) (Supplementary Data Fig. S1). A cardiac-gated two-dimensional phase-contrast MRI (PC-MRI) was done to estimate temporal changes in blood flow volume at the right CCA proximal to the bifurcation during a cardiac cycle (Supplementary Data Fig. S2A–C) (13). A distribution ratio of blood flow volume at the distal to the bifurcation was determined by noncardiac-gated three-dimensional PC-MRI (Supplementary Data Fig. S2D, E and Supplementary Data Materials and Methods).

Assessments of Regions Presenting Focal Growth

A total of 10 aneurysm lesions were subjected to sequential MRA examination. MRA examinations on the 5th, 10th, 17th, and 30th days after the surgery were planned in 7 aneurysm lesions to disclose the time course of the development and growth of induced aneurysms. In the other 3 lesions, MRA examinations on the 12th and 14–15th days after the surgery were performed for macrophage imaging described in the following section.

Regions showing focal growth in induced aneurysms were determined by comparing MRA data obtained at 2 different time points between the 10th and 17th day after surgical manipulation. We validated the growing regions by overlaying the 2 images three-dimensionally according to the methods previously reported (14). Briefly, the regions of aneurysms and the bilateral CCAs were extracted by thresholding the image intensity and removing unnecessary regions. Then, image registration was performed on the images of the 2 different time points. For visualization, surface data were created and overlaid (14). The surface area of each aneurysm lesion was divided into 2 regions: A stable region and a growing one. The region where the 2 MRA overlapped each other was defined as the stable one and the other as a growing one (Supplementary Data Materials and Methods).

Macrophage Imaging by Ferumoxytol

Macrophage imaging by iron-containing nanoparticles, ferumoxytol (Feraheme, AMAG Pharmaceuticals, Waltham, MA) was performed in 3 aneurysm lesions (15, 16). After detecting aneurysm lesions on the 12th day after the surgery, a bolus of ferumoxytol (50 mg/kg) was administered intravenously. At 48–72 hours after the administration of ferumoxytol, MRI experiments of 3D TOF-MRA and T2*W imaging were performed to detect morphological changes from the previous MRA and the uptake of ferumoxytol in the lesions. The T2*W image acquired here depicts the distribution of ferumoxytol as hypointense areas. To clarify the area where the ferumoxytol accumulates, we overlaid the MRA image on the T2*W image (Supplementary Data Materials and Methods).

After the MRI experiments, rats were killed, and sections were prepared as described above. Berlin blue staining was performed to visualize iron deposition derived from ferumoxytol according to manufacturer instructions (Berlin Blue Staining Set, Wako Pure Chemical Corporation, Osaka, Japan).

CFD Analysis

Information on intraluminal surfaces of the artery was obtained from MRA with a commercially available imaging software AMIRA ver. 5.4.2 (Thermo Fisher Scientific, Waltham, MA). Blood was assumed to be an incompressible Newtonian fluid with a density of 1.06×10^3 kg/m^3 and dynamic viscosity of 4.0×10^{-3} Pa s. Unsteady hemodynamics was simulated with the commercial CFD program (scFLOW v2020, Cradle Co, Tokyo, Japan). A flow rate at the inlet measured by cardiac-gated two-dimensional PC-MRI was used. A flow distribution ratio in each outlet was estimated by noncardiac-gated three-dimensional PC-MRI, if available, or otherwise, according to Murray's law (17). The following hemodynamic parameters were analyzed: Time-averaged wall shear stress (TAWSS) (18), WSS at peak systole (WSS_{sys}), WSS at end-diastole (WSS_{dia}), oscillatory shear index (OSI) (19), and time-averaged WSS divergence (TAWSSD) (20).

In each aneurysm lesion, the distributions of these parameters on regional maps were qualitatively compared between growing region and stable regions. The spatial average of these parameters over the growing region, the stable region, and the parent artery in each aneurysm were calculated and quantitatively compared (Supplementary Data Materials and Methods).

Statistics

Continuous variables are presented as the median and interquartile range. Differences between 2 groups were examined using the nonparametric Wilcoxon rank-sum test. Nonparametric multiple comparisons were conducted using the Steel-Dwass test. Statistical comparisons for repeated measurement data were performed by repeated measures analysis

of variance. A scatter diagram with linear regression lines were presented to investigate the correlation between TAWSS and OSI. A p value <0.05 was defined as statistically significant. All statistical analyses were performed with JMP software, version 14.0 (SAS Institute, Cary, NC).

RESULTS

Incidence and Size of Induced Aneurysms

No sham-operated animals developed aneurysms (n = 6, Supplementary Data Fig. S3A, B). At one month after surgical manipulations, de novo saccular aneurysms at the surgically created CCA bifurcation were induced (Fig. 1C and Supplementary Data Fig. S3C). These results indicated that the pathogenesis of aneurysms induced in the present model presumably depends on the morphology of the artery (i.e. the bifurcation site) and hemodynamic force loaded there. Perioperative mortality rate (death within one week after the manipulation) was 28.6% (18/63 animals). A remaining 45 animals were included in the present analysis. The incidence of aneurysms was 44% (20/45 animals). Among the 20 aneurysm lesions, morphological data by MRA were available in 17. The median size of them was 3.2 mm (interquartile range, 2.4–4.3 mm, n = 17) (Fig. 1D). Systolic blood pressure of animals with (n = 5) or without (n = 8) aneurysms was similar (Supplementary Data Fig. S4).

Histological Similarities to Human IAs in the Present Model

Immunofluorescent staining of CD31 and a α-smooth muscle actin demonstrated the presence of 3 layers of arterial walls (i.e. the intima, the media, and the adventitia) (Fig. 2A), confirming the induction of true aneurysms. In past studies, the disruption of the internal elastic lamina and the presence of degenerative or proliferative changes in the media have been considered the hallmarks of human IAs (21–23). Elastic van Gieson staining revealed that induced aneurysms mimicked human IAs (Fig. 2B, C). Additionally, the infiltration of CD68-positive macrophages and the activation of NF-κB, which mediates the growth of IAs (7–10, 22, 23), could be observed (Fig. 2D, E and Supplementary Data Fig. S5). Inducible nitric oxide synthase was induced in the media of aneurysmal walls, as in human IAs (Fig. 2F) (24). The quantitative assessment demonstrated that the infiltration of CD68-positive cells, the activation of NF-κB, and the expression of inducible nitric oxide synthase were more abundant in induced aneurysms (n = 5) than in the bifurcation site without aneurysms (n = 5) (Supplementary Data Fig. S6).

Growth of Induced Aneurysms

There were significant increases in the blood flow volume at peak-systole and mean in a cardiac cycle through the right CCA between the 5th and 30th day postoperatively (n = 8, Fig. 3A). Induced aneurysms rapidly enlarged between the 5th and 10th day, and subsequently gradually enlarged as assessed by 3D TOF-MRA (n = 7, Fig. 3B).

Rupture of Induced Aneurysms

Sudden death due to aneurysmal rupture was observed in some animals. The rupture mostly occurred between the 10th and 15th day after the surgery. The cumulative rupture rate during the first 30 days was 38.9% (7/18 animals) (Fig. 3C). Elastic van Gieson staining revealed thin arterial walls around the rupture point (Fig. 3D). The immunohistochemical examination also confirmed the degenerative changes including disorganized alignment in the medial smooth muscle layers and the accumulation of CD68-positive macrophages near the rupture point (Fig. 3E). In past studies, myeloperoxidase-positive cells, mainly neutrophils (25), and the expression of matrix metalloproteinase 9 have been shown to be involved in the process leading to rupture of human IAs (26, 27). In the present model, myeloperoxidase-positive cells infiltrated in the ruptured lesions and expressed matrix metalloproteinase 9 (Fig. 3F). The quantitative assessment revealed that the density of myeloperoxidase-positive cells and matrix metalloproteinase 9 expressing cells were both increased in ruptured aneurysms than in unruptured ones (Supplementary Data Fig. S7). The size of the aneurysms was similar between ruptured and unruptured aneurysms (Supplementary Data Fig. S7).

Hemodynamic Parameters Associated With Focal Growth of Aneurysms

We assessed the growth of induced aneurysms using morphological data at 2 different time points between the 10th and 17th day after the induction. Among the 10 aneurysms subjected to sequential MRA examinations, we identified focal growth in 5, growth in the whole lesion in 2, and no growth in one. We could not evaluate growth in 2 aneurysms because of death due to the rupture of the lesions (Fig. 3B). We, therefore, subjected the 5 aneurysms to the assessments of hemodynamic parameters associated with the focal growth. Among TAWSS, OSI, and TAWSSD, the areas exposed to low TAWSS colocalized with the growing regions (Fig. 4A). The regions exposed to high OSI colocalized with the growing regions in 4 of the 5 (Supplementary Data Fig. S9). Quantitative assessment revealed that TAWSS and WSS_{sys} were significantly lower in the growing regions than in the stable ones or the parent arteries, whereas these were similar in the stable ones and the parent arteries (Fig. 4B). At the baseline before the aneurysm induction on the 5th day after the surgery, WSS_{sys} was significantly higher at the bifurcation site than the parent artery (Supplementary Data Fig. S8). In a scatter diagram investigating correlation between TAWSS and OSI, the growing regions, the stable ones of aneurysm lesions, and the parent arteries were distributed differently (Supplementary Data Fig. S10). Furthermore, the low OSI characterized the parent artery, whereas low WSS was characteristic of the growing regions (Supplementary Data Fig. S10).

Macrophage Infiltration in Growing and Low WSS-Loaded Regions

We performed macrophage imaging by ferumoxytol in 3 aneurysm lesions. The macrophage imaging revealed that

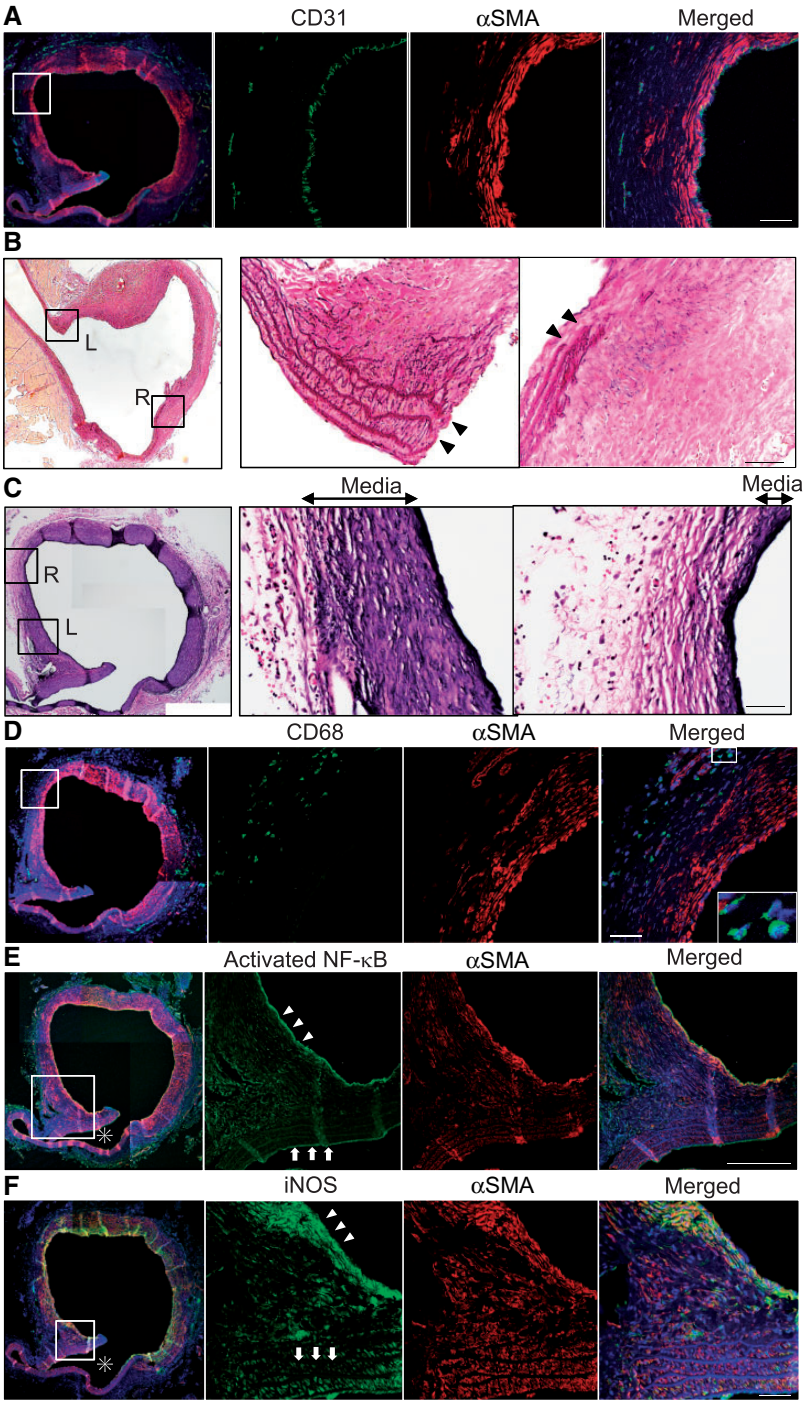

FIGURE 2. The histopathological evaluation of induced aneurysms. **(A)** Representative images of immunofluorescent staining for an endothelial cell marker, CD31 (green), a smooth muscle cell marker, α-smooth muscle actin (αSMA, red), nuclear staining by DAPI (blue), and the merged image. Scale bar: 50 μm. **(B, C)** Elastic van Gieson staining demonstrating the disruption of the internal elastic laminas (indicated by arrowheads in **[B]**) and thickening or thinning of the media **(C)**. The magnified images corresponding to the squares in the left panels are shown on the right. L, the left panel in the magnified images; R, the right panel in the magnified images. Scale bar: 50 μm. **(D–F)** Representative images of immunofluorescent staining for a macrophage marker, CD68 **(D)** (green), activated NF-κB **(E)** (green), iNOS **(F)** (green), αSMA (red), nuclear staining by DAPI (blue), and the merged images. The magnified images corresponding to the squares in the left panels are shown on the right. A further magnified image corresponding to the white square in the right panel in **(D)** is also shown in the bottom right-hand corner of the same panel. The arrowheads in **(E)** indicate the activation of NF-κB in the intima and inner layers of the media in the lesion. The arrowheads in **(F)** indicate the induction of iNOS in the medial smooth muscle cell layers in the lesion. The arrows in **(E, F)** indicate the activation of NF-κB or the expression of iNOS in the parent artery. The asterisks in **(E, F)** indicates the parent artery. Scale bar: 50 μm.

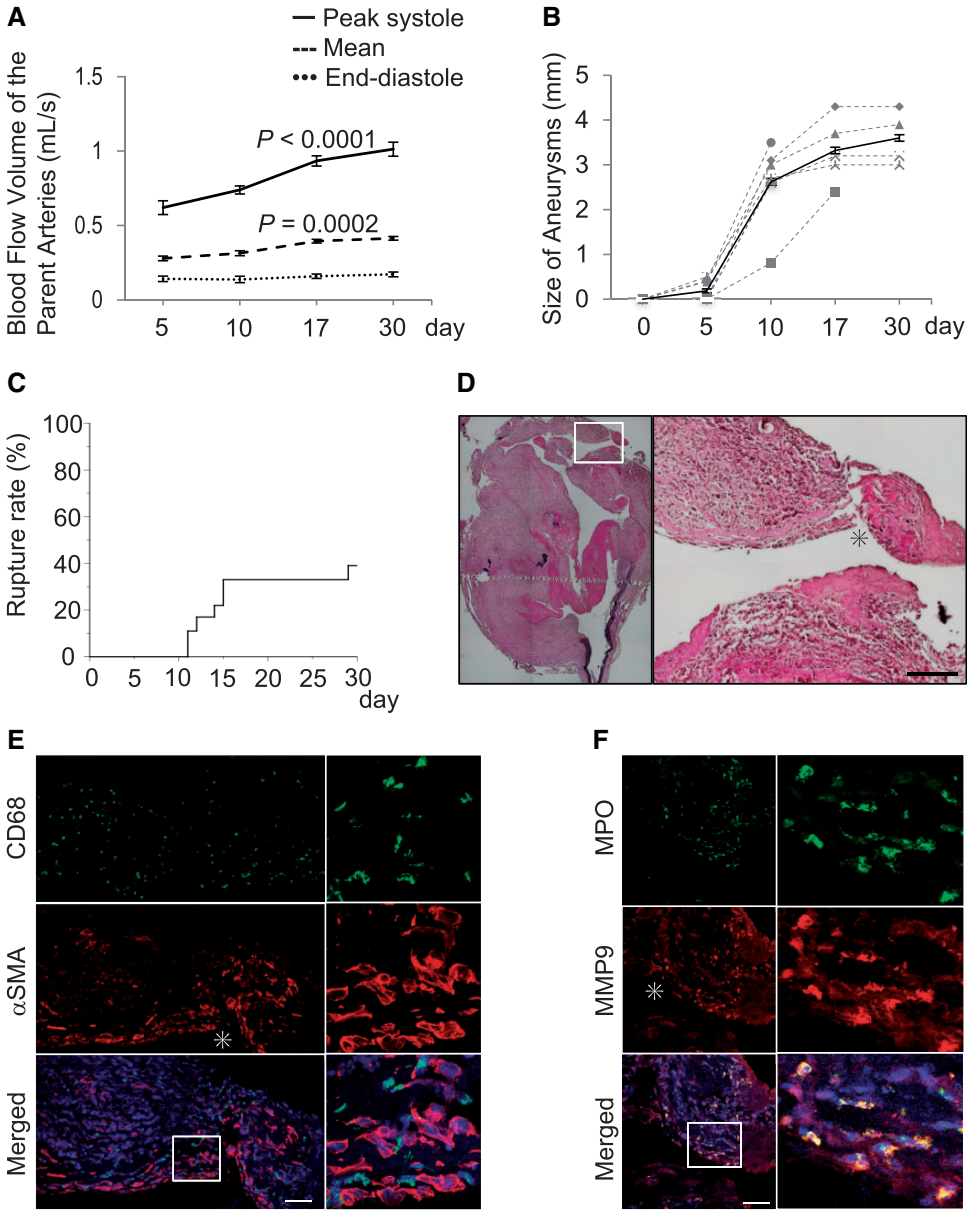

FIGURE 3. Growth and rupture of induced aneurysms. **(A)** Sequential assessments of the blood flow volume at the right common carotid artery proximal to the bifurcation measured by cardiac-gated two-dimensional phase contrast-MRI. Data represent the mean ± SEM (n = 8). Statistical analyses were done by repeated measurement analysis of variance. **(B)** The growth of induced aneurysms assessed by 7-T MR angiography (n = 7). The growth curve of each aneurysm lesion is shown with dotted lines and their mean ± SEM with a continuous line. **(C)** The rupture rate of induced aneurysms (n = 18). **(D)** Representative histopathological images by Elastic van Gieson staining of a ruptured aneurysm. The magnified images corresponding to the squares are shown on the right. The asterisk in **(D)** indicates the point of rupture. Scale bar: 50 μm. **(E, F)** Representative images of immunostaining for a macrophage marker, CD68 **(E)** (green), α-smooth muscle actin (αSMA) **(E)** (red), myeloperoxidase (MPO) **(F)** (green), matrix metalloproteinase 9 (MMP9) **(F)** (red), nuclear staining by DAPI (blue), and the merged images. The magnified image corresponding to the square in **(F)** is shown on the right. The asterisks indicate the point of rupture. Scale bar: 50 μm.

hypo-intense areas demonstrating macrophage infiltration were specifically observed in the growing regions exposed to low WSS and high OSI (Fig. 5A–C). Berlin blue staining and immunofluorescent staining of the sections confirmed the accumulation of ferumoxytol-labeled CD68-positive macrophages in the same area (Fig. 5D–F).

DISCUSSION

We established a rat aneurysm model by surgically creating a bifurcation site at the CCA. The increase of blood flow at the site of the bifurcation was induced by the combination of sodium retention and flow alteration. Therefore, the concept that high flow condition triggers expansive outward vessel

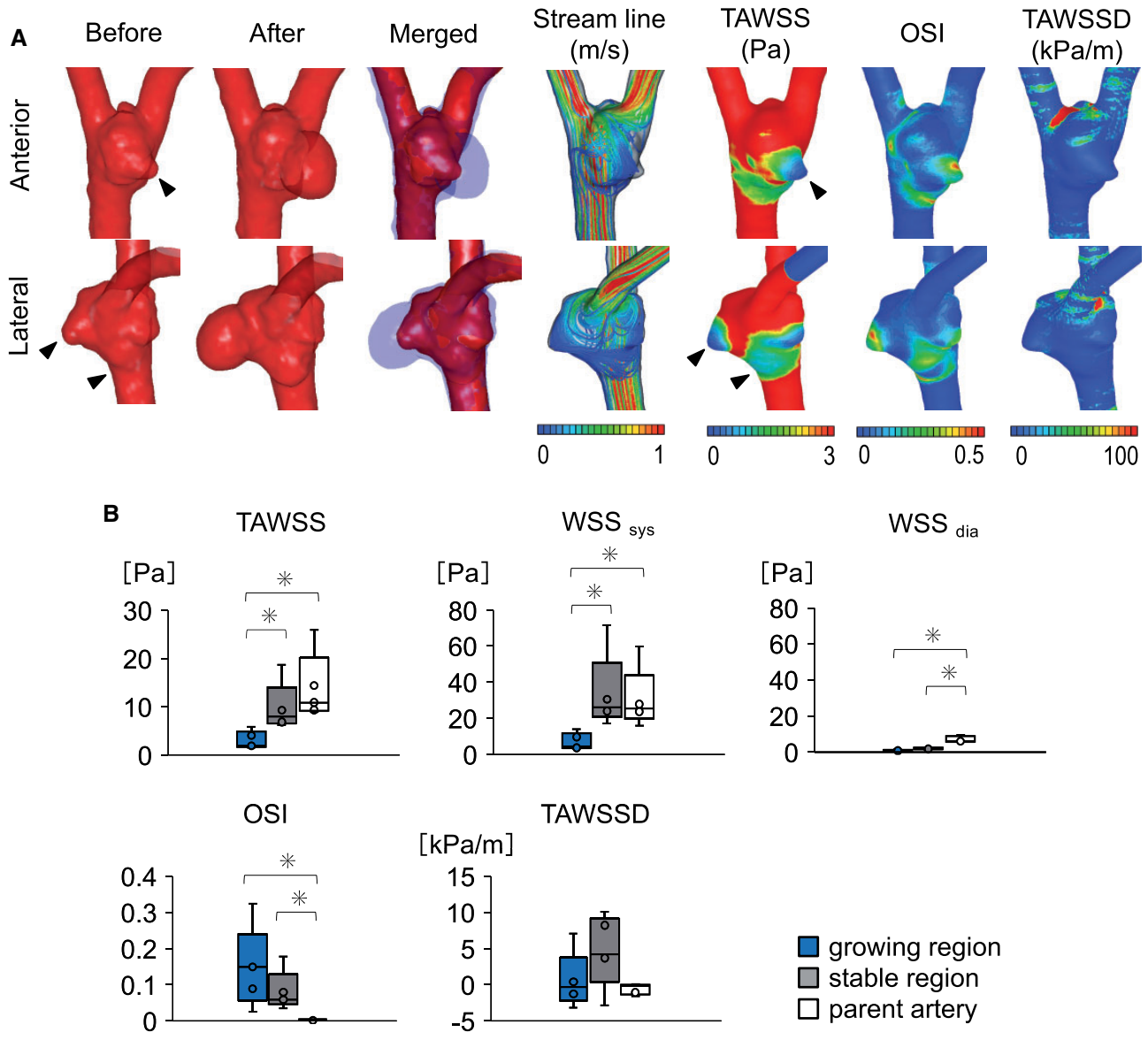

FIGURE 4. Colocalization of growth and hemodynamic parameters in induced aneurysms. **(A)** Representative morphological images and regional maps of CFD parameters in the corresponding case. Arrowheads indicate the growing regions in the aneurysm lesion. TAWSS, time-averaged wall shear stress; OSI, oscillatory shear index; TAWSSD, time-averaged wall shear stress divergence. **(B)** The quantitative comparisons of hemodynamic parameters between the growing, the stable regions of aneurysm lesions, and the parent arteries. The values of hemodynamic parameters by spatial average were calculated in each region. Data are shown in box-and-whisker plots (n = 5). Statistical analyses were done by the nonparametric Steel-Dwass test. WSS_{sys}, WSS at peak systole; WSS_{dia}, WSS at end-diastole.

remodeling was also applied in the present model (28). Using this model, we could evaluate the morphology of induced aneurysms by 7-T MRA. The morphological and histopathological findings of induced aneurysms mimicked those of human IAs. Additionally, immunohistochemical assessments revealed close similarities regarding the inflammatory responses between aneurysms in the present model and IAs. Importantly, the growth curves of induced aneurysms were similar among the animals investigated. Such homogeneity of the disease progression in the current model enables us to analyze the mechanisms regulating each step of the disease by selecting periods after the induction. We could indeed efficiently detect the focal growth of induced aneurysms and qualitatively identified low WSS and high OSI as hemodynamic factors potentially facilitating the focal growth. Interestingly, the quantitative assessment of these hemodynamic parameters revealed that the values of WSS in stable regions were close to those in the parent arteries, suggesting that the stable regions

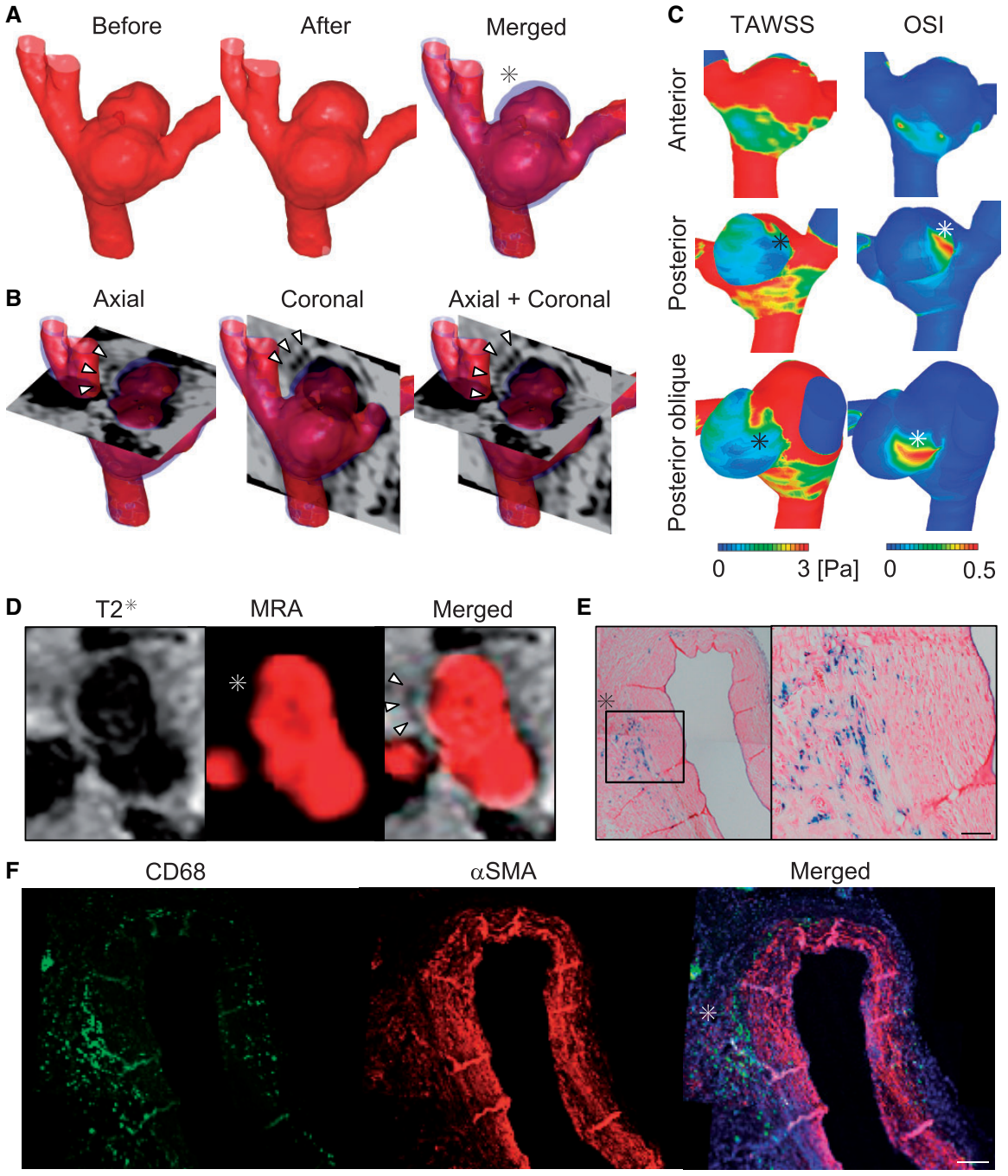

FIGURE 5. Colocalization of growth, hemodynamic parameters, and macrophage infiltration in induced aneurysms. **(A)** Representative images showing a growing region identified by comparing 2 sequentially acquired MR angiographies (MRA). **(B)** Accumulation of macrophages demonstrated by macrophage imaging using ferumoxytol in the corresponding case. An axial (left panel), a coronal (middle panel), and the both of the planes (right panel) by T2*images are shown. The arrowheads in **(B)** indicate hypointense signals in the T2*images showing the accumulation of macrophages. **(C)** Regional maps of TAWSS and OSI of the corresponding case. TAWSS, time-averaged wall shear stress; OSI, oscillatory shear index. **(D)** The axial plane of the T2*-weighted image, time-of-flight MRA, and the merged image corresponding to those presented in **(B)**. Arrowheads in the merged image indicate hypo-intensity areas in the T2*-weighted image reflecting ferumoxytol accumulation. **(E)** Detection of ferumoxytol-labeled macrophages visualized by Berlin blue staining using the specimen from the same animal shown in **(A–D)**. The magnified image corresponding to the squares is shown on the right. Scale bar: 50 μm. **(F)** Representative images of immunofluorescent staining for a macrophage marker, CD68 (green), α-smooth muscle actin (αSMA) (red), nuclear staining by DAPI (blue), and the merged image. Scale bar: 200 μm. The asterisks in **(A–F)** indicate the growing regions.

were exposed to more physiological hemodynamic conditions than the growing regions. Meanwhile, the WSS loaded at the bifurcation site before the aneurysm formation was different from that at the growing region of induced aneurysms. The pathogenesis of the initiation and the focal growth of already-formed aneurysms may thus be a different phenomenon. Furthermore, macrophage imaging by ferumoxytol suggested that the area showing macrophage infiltration colocalized with the growing regions. These findings suggest that growth, hemodynamic forces, and macrophage infiltration may mutually be related in the process of disease progression.

There have been several murine IA models established thus far (29–32). Through a series of experiments using these animal IA models, macrophage-mediated chronic inflammation has been identified as a cardinal driver of the initiation and growth of IAs (8–10, 33). More recently, murine IA models that frequently develop aneurysmal subarachnoid hemorrhage have also been established, for example, by modifying the pattern of arterial ligations and the sex used (31, 32); thus, molecular mechanisms underlying ruptures can be investigated. Interestingly, the rupture rate of the present model was similar to those of already-established IA models (i.e. ∼30%–50%), which may indicate the similarity in the pathogenesis between them. However, because of the small size of intracranial arteries, radiological assessments by MRA were technically difficult in these IA models. Several extracranial aneurysm models have thus been developed because of their size merit compared with intracranial models (34). However, there have been few extracranial aneurysm models that could induce de novo aneurysms and visualize the whole process of morphological changes from the development by MRA. Furthermore, macrophages infiltrating into lesions could also be visualized by macrophage imaging in the present model. Consequently, CFD analyses to clarify the hemodynamic parameters related to the macrophage-mediated inflammation in aneurysms have become more practical. Accordingly, our present model broadens the application of animal models in the research field.

The understanding of mechanisms underlying the growth of IAs is clinically relevant because the rupture rate of human IAs presenting growth is >10 times higher than that for ones without growth (5, 6). However, in humans, the growth of lesions during the follow-up period is infrequent, that is, ∼5%–8% per year (5, 6), and the detection of the growth is time-consuming. There are indeed only a few reports analyzing the hemodynamic parameters related to the growth of human IAs (35, 36). In the present model, we could qualitatively identify the colocalization of the hemodynamic conditions of low WSS and presumably high OSI with the growing regions. In in vitro experiment, chemoattractants for macrophages like monocyte chemoattractant protein-1 were induced in endothelial cells exposed to low WSS and the concomitant turbulent flow (37). Consistently, in this study, macrophage infiltration into aneurysm lesions occurred around the area exposed to the similar hemodynamic condition. Past studies have suggested the facilitation of the growth of IAs via macrophage-mediated chronic inflammation (8–10); for instance, the administration of a dominant-negative form of monocyte chemoattractant protein-1, 7-ND, suppressed the growth of IAs in a rat model (10). Thus, macrophages accumulated in lesions of the present model supposedly regulate the focal growth via regulating the inflammatory response in situ. These findings suggest that detecting these hemodynamic conditions or macrophage infiltration into lesions could be markers identifying unstable lesions and may thus be useful in deciding indication of the treatment.

The present study suggests that exposure to low WSS predisposed to the focal growth of saccular aneurysms. In this regard, another arterial disease, atherosclerosis, has also been considered to be promoted under low WSS (38). These 2 arterial pathophysiologies may develop under similar hemodynamic conditions in terms of WSS. However, one of the hallmarks of atherosclerosis, neointimal hyperplasia, was not observed in the growing regions of saccular aneurysms. These facts may imply another hemodynamic factor other than low WSS mediates the difference between these 2 vascular abnormalities. Hemodynamic factors discriminating between these 2 arterial diseases should be further clarified.

There are several limitations to the present study. First, there are differences in the structure between intracranial arteries and the CCA. For instance, the elastic lamina is monolayer in intracranial arteries, whereas it is multilayer in the CCA. Such differences may influence the pathogenesis by affecting the stiffness of arterial walls and the recruitment of inflammatory cells. Second, although the regions exposed to high OSI qualitatively colocalized with the growing ones, the quantitative analysis failed to detect a statistical difference in the values of OSI between the stable and the growing regions. We used OSI as an indicator of turbulent flow, but turbulent flow includes various types of flow conditions other than laminar flow. Indeed, there are several other parameters demonstrating turbulent flow, such as the gradient oscillatory number (39). Further investigations to identify a parameter more accurately reflecting turbulent flow and most effectively evoking cellular responses are necessary to answer these questions.

In conclusion, we propose an extracranial aneurysm model that visualizes sequential morphological changes of de novo aneurysms by MRA. The CFD analysis using the present aneurysm model suggests the colocalization of the areas exposed to low WSS and high OSI with the growing regions of aneurysm lesions. Macrophage imaging by ferumoxytol shows the accumulation of macrophages in the growing regions. These findings imply the potential contribution of low WSS and high OSI to the macrophage-mediated growth of saccular aneurysms. Therefore, this study provides further support that the growth of saccular aneurysms is triggered by specific hemodynamic stimulus promoting inflammatory responses in aneurysm lesions.

REFERENCES

1. Davis FM, Daugherty A, Lu HS. Updates of recent aortic aneurysm research. Arterioscler Thromb Vasc Biol 2019;39:e83
2. Pitton MB, Dappa E, Jungmann F, et al. Visceral artery aneurysms: Incidence, management, and outcome analysis in a tertiary care center over one decade. Eur Radiol 2015;25:2004–14
3. Vlak MH, Algra A, Brandenburg R, et al. Prevalence of unruptured intracranial aneurysms, with emphasis on sex, age, comorbidity, country, and

time period: A systematic review and meta-analysis. Lancet Neurol 2011;10:626–36
4. Nieuwkamp DJ, Setz LE, Algra A, et al. Changes in case fatality of aneurysmal subarachnoid haemorrhage over time, according to age, sex, and region: A meta-analysis. Lancet Neurol 2009;8:635–42
5. Teo M, St George EJ. Radiologic surveillance of untreated unruptured intracranial aneurysms: A single surgeon's experience. World Neurosurg 2016;90:20–8
6. Villablanca JP, Duckwiler GR, Jahan R, et al. Natural history of asymptomatic unruptured cerebral aneurysms evaluated at CT angiography: Growth and rupture incidence and correlation with epidemiologic risk factors. Radiology 2013;269:258–65
7. Aoki T, Kataoka H, Shimamura M, et al. NF-kappaB is a key mediator of cerebral aneurysm formation. Circulation 2007;116:2830–40
8. Aoki T, Frősen J, Fukuda M, et al. Prostaglandin E2-EP2-NF-κB signaling in macrophages as a potential therapeutic target for intracranial aneurysms. Sci Signal 2017;10:eaah6037
9. Kanematsu Y, Kanematsu M, Kurihara C, et al. Critical roles of macrophages in the formation of intracranial aneurysm. Stroke 2011;42:173–8
10. Aoki T, Kataoka H, Ishibashi R, et al. Impact of monocyte chemoattractant protein-1 deficiency on cerebral aneurysm formation. Stroke 2009;40:942–51
11. Can A, Du R. Association of hemodynamic factors with intracranial aneurysm formation and rupture. Neurosurgery 2016;78:510–20
12. Metaxa E, Tremmel M, Natarajan SK, et al. Characterization of critical hemodynamics contributing to aneurysmal remodeling at the basilar terminus in a rabbit model. Stroke 2010;41:1774–82
13. Peng S-L, Shih C-T, Huang C-W, et al. Optimized analysis of blood flow and wall shear stress in the common carotid artery of rat model by phase-contrast MRI. Sci Rep 2017;7:5253
14. Jenkinson M, Bannister P, Brady M, et al. Improved optimization for the robust and accurate linear registration and motion correction of brain images. Neuroimage 2002;17:825–41
15. Hasan DM, Mahaney KB, Magnotta VA, et al. Macrophage imaging within human cerebral aneurysms wall using ferumoxytol-enhanced MRI: A pilot study. Arterioscler Thromb Vasc Biol 2012;32:1032–8
16. Shimizu K, Kushamae M, Aoki T. Macrophage Imaging of Intracranial Aneurysms. Neurol Med Chir (Tokyo) 2019;59:257–63
17. Murray CD. The physiological principle of minimum work applied to the angle of branching of arteries. J Gen Physiol 1926;9:835–41
18. Geers AJ, Morales HG, Larrabide I, et al. Wall shear stress at the initiation site of cerebral aneurysms. Biomech Model Mechanobiol 2017;16:97–115
19. Ku DN, Giddens DP, Zarins CK, et al. Pulsatile flow and atherosclerosis in the human carotid bifurcation. Positive correlation between plaque location and low oscillating shear stress. Arteriosclerosis 1985;5:293–302.
20. Zhang Y, Takao H, Murayama Y, et al. Propose a wall shear stress divergence to estimate the risks of intracranial aneurysm rupture. Sci World J 2013;2013:1–8
21. Hashimoto N, Handa H, Hazama F. Experimentally induced cerebral aneurysms in rats: Part III. Pathology. Surg Neurol 1979;11:299–304
22. Frösen J, Piippo A, Paetau A, et al. Remodeling of saccular cerebral artery aneurysm wall is associated with rupture: Histological analysis of 24 unruptured and 42 ruptured cases. Stroke 2004;35:2287–93
23. Kataoka K, Taneda M, Asai T, et al. Structural fragility and inflammatory response of ruptured cerebral aneurysms. A comparative study between ruptured and unruptured cerebral aneurysms. Stroke 1999;30:1396–401
24. Fukuda S, Hashimoto N, Naritomi H, et al. Prevention of rat cerebral aneurysm formation by inhibition of nitric oxide synthase. Circulation 2000;101:2532–8
25. Lau D, Baldus S. Myeloperoxidase and its contributory role in inflammatory vascular disease. Pharmacol Ther 2006;111:16–26
26. Chu Y, Wilson K, Gu H, et al. Myeloperoxidase is increased in human cerebral aneurysms and increases formation and rupture of cerebral aneurysms in mice. Stroke 2015;46:1651–6
27. Gounis MJ, Vedantham S, Weaver JP, et al. Myeloperoxidase in human intracranial aneurysms: Preliminary evidence. Stroke 2014;45:1474–7
28. Frösen J, Cebral J, Robertson AM, et al. Flow-induced, inflammation-mediated arterial wall remodeling in the formation and progression of intracranial aneurysms. Neurosurg Focus 2019;47:E21
29. Hashimoto N, Handa H, Hazama F. Experimentally induced cerebral aneurysms in rats. Surg Neurol 1978;10:3–8
30. Marbacher S, Marjamaa J, Bradacova K, et al. Loss of mural cells leads to wall degeneration, aneurysm growth, and eventual rupture in a rat aneurysm model. Stroke 2014;45:248–54
31. Miyamoto T, Kung DK, Kitazato KT, et al. Site-specific elevation of interleukin-1β and matrix metalloproteinase-9 in the Willis circle by hemodynamic changes is associated with rupture in a novel rat cerebral aneurysm model. J Cereb Blood Flow Metab 2017;37:2795–805
32. Nuki Y, Tsou T-L, Kurihara C, et al. Elastase-induced intracranial aneurysms in hypertensive mice. Hypertension 2009;54:1337–44
33. Shimizu K, Kushamae M, Mizutani T, et al. Intracranial aneurysm as a Macrophage-mediated inflammatory disease. Neurol Med Chir (Tokyo) 2019;59:126–32
34. Marbacher S, Strange F, Frösén J, et al. Preclinical extracranial aneurysm models for the study and treatment of brain aneurysms: A systematic review. J Cereb Blood Flow Metab 2020;40:922–38
35. Sforza DM, Kono K, Tateshima S, et al. Hemodynamics in growing and stable cerebral aneurysms. J NeuroIntervent Surg 2016;8:407–12
36. Leemans EL, Cornelissen BMW, Slump CH, et al. Comparing morphology and hemodynamics of stable-versus-growing and grown intracranial aneurysms. Am J Neuroradiol 2019;40:2102–10.
37. Aoki T, Yamamoto K, Fukuda M, et al. Sustained expression of MCP-1 by low wall shear stress loading concomitant with turbulent flow on endothelial cells of intracranial aneurysm. Acta Neuropathol Commun 2016;4:48
38. Portanova A, Hakakian N, Mikulis DJ, et al. Intracranial vasa vasorum: Insights and implications for imaging. Radiology 2013;267:667–79
39. Shimogonya Y, Ishikawa T, Imai Y, et al. Can temporal fluctuation in spatial wall shear stress gradient initiate a cerebral aneurysm? A proposed novel hemodynamic index, the gradient oscillatory number (GON). J Biomech 2009;42:550–4